Strain-promoted conductive metal-benzenhexathiolate frameworks for overall water splitting

Xiting Wang[a], Huan Niu[a], Xuhao Wan[a], Zhaofu Zhang[b], Ryan Feng Wang[c], Yuzheng Guo[a, *]

[a] *School of Electrical Engineering and Automation, Wuhan University, Wuhan, 430072, Hubei, China*

[b] *Department of Engineering, University of Cambridge, Cambridge, CB2 1PZ, United Kingdom*

[c] *Departments of Chemical Engineering, University College London, Torrington Place, London WC1E 7JE, UK*

***Corresponding Author.**

E-mail address: yguo@whu.edu.cn (Y. Guo)

Abstract

Designing efficient catalysts for hydrogen evolution reaction (HER) and oxygen evolution reaction (OER) is a desirable strategy for overall water splitting and the generation of clean and renewable energies. Herein, the electrocatalytic HER and OER activity of the conductive metal-benzenhexathiolate (M-BHT) frameworks has been evaluated utilizing first-principles calculations. The in-plane π-d conjugation of M-BHT guarantees fast electron transfer during electrocatalytic reactions. Notably, Rh-BHT holds the promise of bifunctional HER/OER activity with the overpotentials of 0.07/0.36 V. Furthermore, the application of strain engineering tailors the adsorption of intermediates and promotes the overall water splitting performance. Rh-BHT with the +1% tensile strain shows the HER/OER overpotential of 0.02/0.37 V. This work not only demonstrates the prospects of conductive metal-organic frameworks in electrocatalysis but also offers new insights into designing efficient catalysts by strain engineering.

Keywords: electrocatalysis, overall water splitting, metal-organic frameworks, strain engineering, first-principles calculations

1. Introduction

As an attractive technology to solve the issues of energy shortage and environmental pollution, electrochemical water splitting can generate clean and sustainable hydrogen (H_2) and oxygen (O_2).[1-3] Traditionally, noble platinum (Pt) and ruthenium/iridium oxides (RuO_2 and IrO_2) are utilized for hydrogen evolution reaction (HER) and oxygen evolution reaction (OER), respectively.[4-8] However, high cost and poor stability hinder the wider application of noble-metal-based catalysts.[5] Many efforts have been paid to find alternative catalysts for HER and OER, e.g., transition metal dichalcogenides for HER,[9, 10] and layer-double-hydroxides and perovskite oxides for OER.[11, 12] It is still a pressing challenge to practically pair the two reactions together in an integrated electrolytic cell, due to their different optimal working conditions.[13] Moreover, preparing different catalysts for HER and OER also brings the duple requirement for equipment and processes.[14-16] Such dilemmas urgently call for constructing high-performance bifunctional HER/OER catalysts to enable overall water splitting.

Metal-organic frameworks (MOFs) possess well-defined periodic and porous structures, which have attracted intensive interest in various applications.[17-21] The crystal structures of MOFs are varied from bulk to two-dimensional (2D) layered structures.[22, 23] With the combination of metal centers and organic linkers, 2D MOFs can be facilely synthesized via bottom-up methods.[24, 25] Numerous metal atoms are uniformly dispersed in 2D MOFs, forming the comparable structures of single-atom catalysts.[26, 27] Whereas, 2D MOFs are usually semiconductive or insulative and cannot guarantee effective transport of electrons, due to the large cavities in the networks.[28, 29]

Recently, the conductive 2D MOFs have been fabricated based on conjugated benzene and triphenylene-based ligands.[30-34] Particularly, as a multidentate ligand with six-fold symmetry, metal-benzenehexathiol (M-BHT) complexes have gained great research interest. The extended in-plane π-d conjugation between metal centers and organic linkers facilitates the delocalization of charge carriers, resulting in the good conductivity of M-BHT.[35] Up to date, some M-BHT frameworks have been successfully synthesized, including Cu-BHT, Fe-BHT, Ag-BHT, and Au-BHT.[35-39] It is noticed that various conductive 2D MOFs have been applied in the field of electrocatalysis.[40-43] For example, $Co_3(HITP)_2$ shows prominent OER activity with the overpotential of 254 mV at 10 mA cm^{-2} in alkaline electrolyte.[40] However, there are rare reports on the M-BHT for electrocatalytic reactions, especially for bifunctional overall water splitting. It is full of interest to address whether M-BHT frameworks are suitable candidates for water splitting and which metal center can exhibit the optimal HER/OER activity.

In this work, the electrocatalytic HER/OER activity of M-BHT (M = Fe, Co, Ni, Cu, Ru, Rh, Pd, Os, Ir, and Pt) was explored to shed light on their potential for overall water splitting. It was demonstrated that M-BHT complexes possessed high stability and good conductivity. Among all M-BHT candidates, Rh-BHT was screened as the attractive bifunctional catalyst for HER/OER with the overpotential of 0.07/0.36 V. Furthermore, the strain-tuning method was applied on Rh-BHT to tailor the catalytic activity. The +1% tensile strained Rh-BHT exhibited boosted water splitting performance with the HER/OER overpotential of 0.02/0.37 V. These findings can guide the exploitation of conductive 2D MOFs and deepen the understanding of strain engineering in electrocatalysis.

2. Computational Methods

Spin-polarized density functional theory (DFT) calculations were executed by using the Vienna *ab initio* simulation package (VASP).[44] The exchange-correlation energy was described by the Perdew-Burke-Ernzerhof (PBE) functional within generalized gradient approximation (GGA).[45] The plane-wave basis was applied with a cutoff energy of 520 eV. The 3 × 3 × 1 Monkhorst-Pack k-point grid was adopted for structural optimization. The 20 Å vacuum thickness was set in the perpendicular direction of the layers to minimize interactions between periodic patterns. To ensure all atomic positions under the fully relaxed states, the convergence criteria of energy and force were set to 10^{-5} eV and 0.02 eV/Å, respectively. The dispersion corrections in Grimme's scheme (DFT-D3) were implemented to describe the long-range van der Waals interactions.[46] The solvation effect was considered by using the implicit solvent model VASPsol.[47] Bader charge analysis was applied to inspect the charge variation.[48] The projected crystal orbital Hamilton population (pCOHP) was employed to reveal the interaction between M-BHT and HER/OER intermediates.[49]

According to the computational hydrogen electrode (CHE) model, the Gibbs free energy change (ΔG) can be calculated by [50, 51]

$$\Delta G = \Delta E + \Delta ZPE - T\Delta S + \Delta U \tag{1}$$

in which ΔE represents the total energy change in DFT calculations. ΔZPE and ΔS are the zero-point energy and entropy corrections at the room temperature of 298.15 K. The *ZPE* and *TS* corrections for intermediates adsorbed on M-BHT are listed in **Table S1**. The effect of the applied electrode potential is corrected by $\Delta U = -eU$, where e and U denote the number of transferred electrons and the applied electrode potential, respectively.

The process of HER is mainly divided into two key steps, the formation of *H and the desorption of H_2. The OER pathway is composed of four elementary steps in acid conditions, following the process of $*+H_2O \rightarrow *OH \rightarrow *O \rightarrow *OOH \rightarrow *+O_2$. The H_2O molecule firstly generates $^*OH$ and one (H^++e^-) pair. In the following step, the $^*OH$ further separates into $^*O$ and forms the second (H^++e^-) pair. Then, the $^*O$ intermediate combines with the H_2O molecule and produces $^*OOH$ and the third (H^++e^-) pair. Finally, the $^*OOH$ dissociates into O_2 with the release of one (H^++e^-) pair. The most considerable elementary step in the whole reaction is called the potential-determining step (PDS). The HER and OER catalytic performance can be assessed by the overpotential (η), which is defined as

$$\eta = \Delta G_{\mathrm{max}} / e - U_{\mathrm{eq}} \quad (2)$$

where ΔG_{max} represents the largest free energy change. U_{eq} is the equilibrium potential of the catalytic reaction. The U_{eq} values for HER and OER are 0 and 1.23 V, respectively.

3. Results and Discussion

3.1 Structure, stability, and electronic property

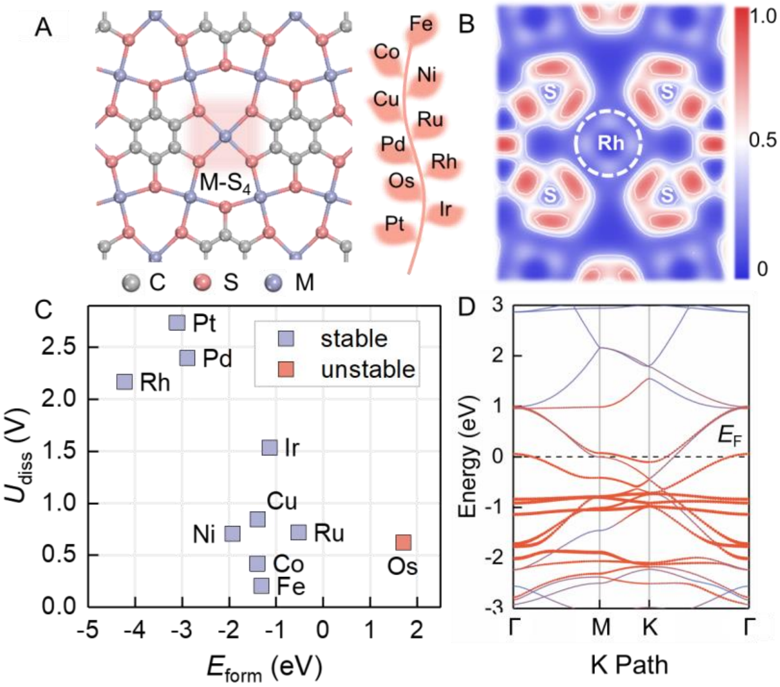

Fig. 1. (a) Configuration of M-BHT and all investigated metal atoms in this work. (b) Electron localization function (ELF) plots of Rh-S_4 interaction in Rh-BHT. (c) Formation energies (E_{form}) and dissolution potentials (U_{diss}) of M-BHT. (d) Projected band structure of Rh-BHT. The Fermi level (E_F) is set to zero.

The structure of M-BHT consists of the benzene ring and M-S_4 center, with the metal atom surrounded by four sulfur atoms (**Fig. 1a**). All investigated metal atoms for M-BHT include Fe, Co, Ni, Cu, Ru, Rh, Pd, Os, Ir, and Pt. As listed in **Table S2**, the lattice parameters of M-BHT complexes range from 8.49 to 8.77 Å with positively charged metal atoms (0.19~0.75 e^-). Electron localization function (ELF) plots of M-BHT are provided in **Fig. 1b** and **Fig. S1** to reveal the bonding characteristics of M-S_4 centers. A high ELF value represents the formation of covalent bonds, while a low ELF value denotes the highly delocalized electrons. The covalent interactions between metal atoms and S atoms prove the strong M-S_4 bonding strength, implying the high stability of the designed M-BHT structures.

Moreover, the feasible catalysts should maintain thermodynamically and electrochemically stable to guarantee the synthesis possibility and long-term durability.[52, 53] The formation energy ($E_{\mathrm{form}} = E_{\mathrm{M\text{-}BHT}} - E_{\mathrm{C6S6H6}} - 3E_{\mathrm{M}} + 6E_{\mathrm{H}}$) is assessed to explore the synthesis possibility of M-BHT. $E_{\mathrm{M\text{-}BHT}}$ and E_{C6S6H6} are the total energies of M-BHT and $C_6S_6H_6$, respectively. E_{M} and E_{H} denote the total energies of the metal atoms in bulk and the half of H_2 in the gas phase, respectively. The negative E_{form} suggests the facile synthesis of M-BHT in experiment. The dissolution potential ($U_{\mathrm{diss}} = U_{\mathrm{diss\text{-}bulk}} - E_{\mathrm{form}}/(n_e e)$) is calculated to evaluate the dissolution possibility of the metal atom on BHT. $U_{\mathrm{diss\text{-}bulk}}$ denotes the standard dissolution potential of bulk metal, and n_e is the number of transferred electrons during dissolution.[54] The positive U_{diss} value is required for an electrochemically stable M-BHT. The detailed E_{form} and U_{diss} values are summarized in **Table S3**. The E_{form} values of most M-BHT are negative (except for Os-BHT) and the U_{diss} values of all M-BHT mentioned above are positive (**Fig. 1c**). The results suggest that only Os-BHT cannot satisfy the criteria of $E_{\mathrm{form}} < 0$ eV and $U_{\mathrm{diss}} > 0$ V. In this regard, we exclude Os-BHT and focus on other M-BHT in the following discussion. Furthermore, the *ab initio* molecular dynamics (AIMD) simulations are performed for the nine M-BHT candidates at 500 K for 10 ps.[55] It is suggested in **Fig. S2** that the total energies of these M-BHT configurations oscillate within small ranges during the AIMD simulations, which further illustrates the stability of M-BHT.

The electronic properties of the catalysts show an important impact on their electrocatalytic performance. The projected band structure of Rh-BHT is plotted in **Fig. 1d** for example to further validate the conductivity of M-BHT. There is a significant contribution of Rh-d orbitals to the electron states near the Fermi level (E_F). The band structures of other M-BHT can be seen in **Fig. S3**. It is revealed that most M-BHT (except for Pt) are metallic with electronic states distributed across the E_F. Thus, the effective orbital interactions between the fully conjugated benzene rings and M-S_4 centers can promote the electron transfer of M-BHT. The good conductivity assures the application of M-BHT in the electrocatalytic HER and OER.

3.2 HER/OER performance

The HER activity of M-BHT is investigated by calculating the hydrogen adsorption energy (ΔG_{*H}), which determines the HER potential-determining step (PDS). Generally, the ΔG_{*H} value of optimal HER catalytic activity is considered zero.[56] The optimized configurations of *H on M-BHT are plotted in **Fig. S4** and the corresponding M-H bond lengths are presented in **Table S4**. The weak H* adsorption leads to the PDS of *H formation on Ni-, Cu-, Pd-, Ir-, and Pt-BHT, while the process of HER is restricted by the release of H_2 on Fe-, Co-, Ru-, and Rh-BHT (**Fig. 2a**). Notably, Rh-BHT possesses the ΔG_{*H} value of -0.07 eV, which is closer to zero than that of commercial Pt (-0.09 eV).[57] This implies that Rh-BHT can act as a promising HER electrocatalyst.

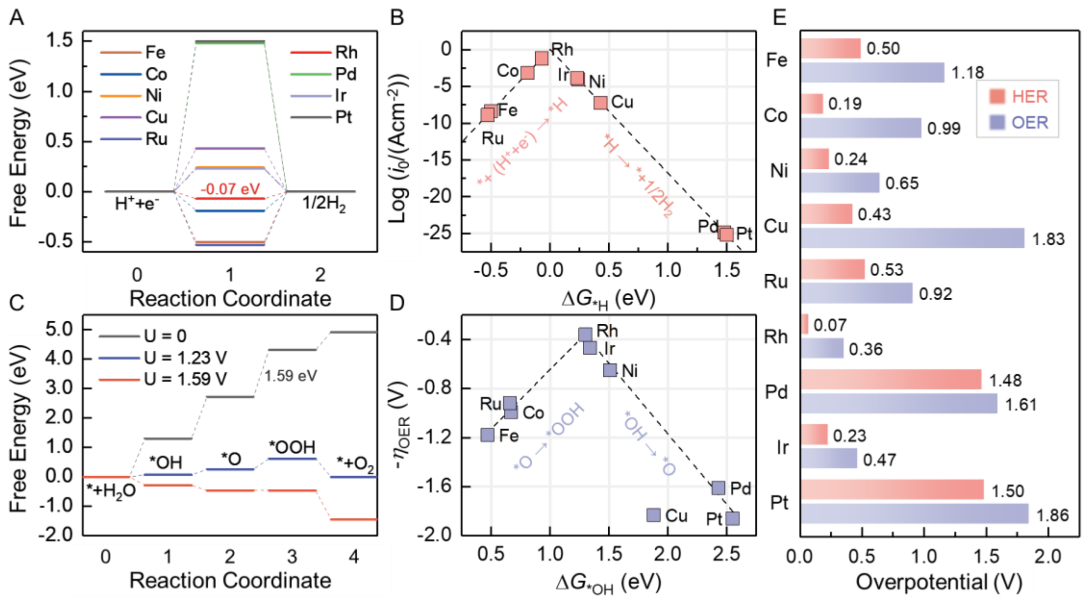

Fig. 2. (a) HER free energy diagrams of M-BHT. (b) Volcano plot for the HER exchange current (i_0) as a function of the hydrogen adsorption energy (ΔG_{*H}) on M-BHT. (c) OER free energy diagrams of Rh-BHT at the applied potential of U = 0, 1.23, and 1.59 V, respectively. (d) Volcano plot for the negative OER overpotential as a function of ΔG_{*OH} on M-BHT. (e) Summarized HER and OER overpotentials of M-BHT.

The HER volcano plot for the exchange current (i_0) as a function of ΔG_{*H} on M-BHT is shown in **Fig. 2b**. Based on Nørskov's assumption, i_0 can be gained according to the calculated ΔG_{*H}, which is expressed as[51]

$$i_0 = -ek_0 \frac{1}{1+\exp(|\Delta G_{*H}|/k_B T)} \quad (3)$$

where k_0 is the rate constant and set to 1.[58, 59] When M-BHT locates at the left branch of the volcano, the desorption of the H_2 molecule becomes the PDS. Constantly, the HER activity is limited by the *H adsorption on the right branch. In particular, Rh-BHT possesses ΔG_{*H} of -0.07 eV and locates near the volcano peak, leading to the maximum i_0 value.

All configurations of the key OER intermediates (*OH, *O, and *OOH) adsorbed on M-BHT can be seen in **Fig. S5-S7**. The adsorption energies of OER intermediates and the corresponding M-O bond lengths on M-BHT are summarized in **Table S5**. The free energy change of each OER elementary step on M-BHT is listed in **Table S6**. The OER free energy diagram of Rh-BHT is plotted in **Fig. 2c**. It is indicated that OER is an endothermic process on Rh-BHT with the energy change of 1.30, 1.42, 1.59, and 0.61 eV for each elementary step at the applied potential of 0 V. The most considerable step for OER is the third step from *O to *OOH. The whole OER process becomes spontaneous until the applied potential of 1.59 V. Therefore, Rh-BHT exhibits the outstanding OER performance with the overpotential (η_{OER}) of 0.36 V, which is lower than that of RuO_2 (η_{OER} = 0.42 V).[60] The OER free energy diagrams of other M-BHT catalysts are shown in **Fig. S8** for comparison.

Fig. 2d presents the OER volcano plot for the OER overpotential as a function of ΔG_{*OH} on M-BHT. The adsorption energy of *OH intermediate is chosen as the descriptor because of the scaling relations between ΔG_{*O} (ΔG_{*OOH}) and ΔG_{*OH} (**Fig. S9**). The OER volcano plot indicates that the strong binding of *OH results in the PDS from *O to *OOH (e.g. Fe-BHT), while the second step (*OH → *O) becomes the PDS when the *OH adsorption is weak (e.g. Pt-BHT). Additionally, the ΔG_{*OH} value of 1.32 eV is required for the optimal OER catalyst. Rh-BHT stands near the OER volcano peak with the ΔG_{*OH} value of 1.30 eV. Moreover, the HER and OER overpotentials (η_{HER} and η_{OER}) on M-BHT are summarized in **Fig. 2e**. It is clarified that Rh-BHT possesses high HER/OER activity with η_{HER}/η_{OER} values of 0.07/0.36 V.

Therefore, the designed Rh-BHT is considered a superior bifunctional HER/OER catalyst.

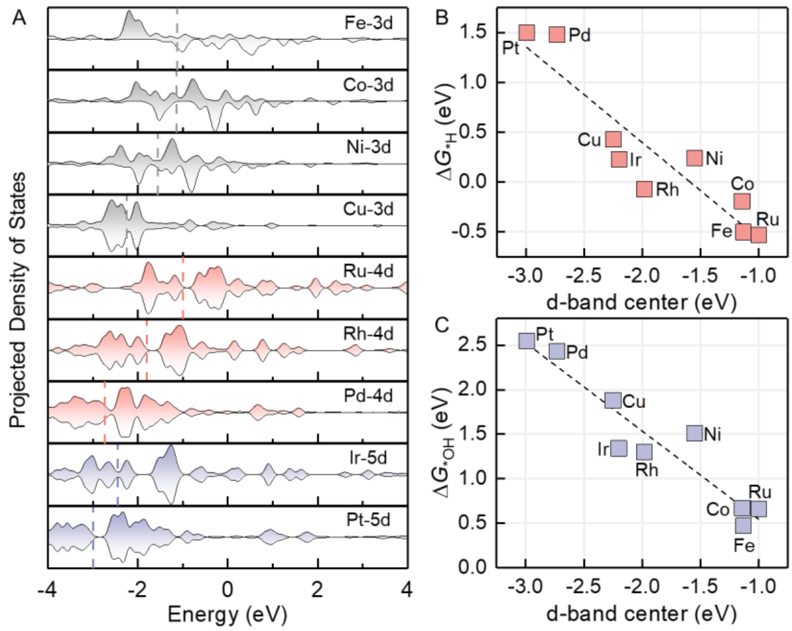

Fig. 3. (a) Partial density of states (PDOS) of d orbitals for M-BHT. The d-band centers (ε_d) are labeled for 3d metal centers (Fe, Co, Ni, and Cu), 4d metal centers (Ru, Rh, and Pd), and 5d metal centers (Ir and Pt). The Fermi level (E_F) is set to 0 eV. (b-c) The adsorption energy of *H and *OH as a function of the d-band center.

During the process of adsorption and reaction, the d orbitals of metal atoms on M-BHT hybridize with the orbitals of intermediates. The HER/OER activity trend is further explored by analyzing the partial density of states (PDOS) of d orbitals on M-BHT (**Fig. 3a**). The d-band center (ε_d) represents the average position of d orbitals, which has been demonstrated as an attractive descriptor to clarify the catalytic activity origin.[61-63] The ε_d value can be calculated as

$$\varepsilon_{\mathrm{d}} = \frac{\int_{-\infty}^{\infty} \varepsilon \rho_{\mathrm{d}} \mathrm{d}\varepsilon}{\int_{-\infty}^{\infty} \rho_{\mathrm{d}} \mathrm{d}\varepsilon} \tag{4}$$

where ρ_d is the d-orbital states of metal atoms on M-BHT. ε is the energy width of the d orbitals. The shift of the d-band center appears with some regularity in each period. That is, the ε_d value gets more negative when the number of d electrons increases. For example, the d-band centers for Ru-, Rh-, and Pd-BHT are -1.00, -1.80, and -2.73 eV, respectively. This trend accounts for the different adsorption strength of intermediates on the different metal centers of M-BHT. The more negative ε_d value corresponds to the weaker adsorption. As seen in **Fig. 3b-c**, the adsorption energy of *H and *OH linearly correlate with the d-band center. Rh-BHT possesses the moderate d-band center and thereby suitable adsorption of intermediates, resulting in the high activity for both HER and OER. Therefore, the analysis of d-band center can provide a quantitative explanation of adsorption behavior and elucidate the HER and OER performance from the aspect of electronic properties.

3.3 Strain effect on HER/OER performance

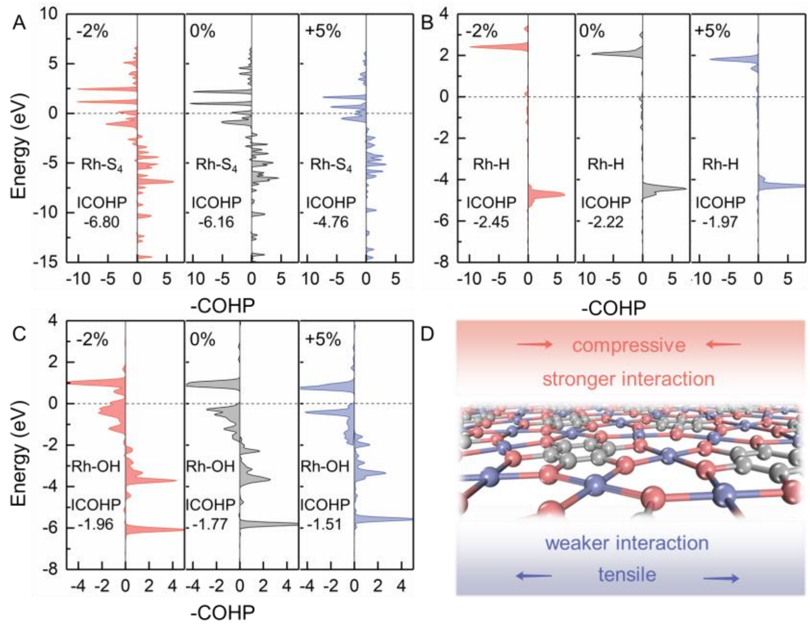

Fig. 4. (a-c) The projected crystal orbital Hamilton population (pCOHP) for the Rh-S_4,

Rh-H, and Rh-OH interaction, respectively. The bonding and antibonding states are drawn on the right and left sides, respectively. The Fermi level (E_F) is set to 0 eV. (d) Illustration of strain effect on Rh-BHT. The compressive strain results in a stronger interaction, while the tensile strain weakens the interaction.

Strain engineering can precisely tune the electronic structures of catalysts and further change the adsorption strength of intermediates, leading to the enhancement of catalytic activity.[64-67] The biaxial strain ($\varepsilon = \Delta a/a_0$) is applied on Rh-BHT to investigate the strain effect on HER/OER activity. Δa denotes the lattice parameter change under the biaxial strain and a_0 is the unstrained lattice constant of Rh-BHT. The strain value ranges from -5% to +5% with an interval of 1%, in which the negative and positive values denote the compressive and tensile strain, respectively. Notably, severe structural distortion is observed when the ε value is from -5% to -3% (**Fig. S10**), implying the unstable configurations of Rh-BHT under the too strong compressive strain. We thus mainly focus on the Rh-BHT with the ε values from -2% to +5%. The relative total energies of fully relaxed configurations under -2% to +5% strain can be seen in **Fig. S11**.

The strain effect on interaction strength can be validated by the projected crystal orbital Hamilton population (pCOHP). **Fig. 4a** presents the pCOHP of the Rh-S_4 interaction, where the bonding and antibonding states are plotted on the right and left sides, respectively. The bonding states gradually move up relative to E_F with the increase of ε value, while the antibonding states shift down. The integrated COHP (ICOHP) can give a quantitative explanation by integrating the energy up to E_F. The more negative ICOHP value corresponds to the stronger interaction. The calculated ICOHP values of Rh-S_4 interaction under ε = -2%, 0%, and +5% are -6.80, -6.16, and -4.76, respectively. This proves the weakened interaction of Rh-S_4 centers when tensile strain increases (compressive strain decreases).

In addition, the strain effect on the adsorption strength of HER and OER intermediates is further assessed. **Fig. 4b-c** suggests that the Rh-H and Rh-OH interaction strength exhibits a similar trend to that of Rh-S_4 centers. Namely, the ICOHP values of Rh-H interaction under ε = -2%, 0%, and +5% are -2.45, -2.22, and -1.97, respectively, while the ICOHP values of Rh-OH interaction with the strain of -2%, 0%, and +5% are -1.96, -1.77, and -1.51, respectively. As illustrated in **Fig. 4d**, the strain effect on Rh-BHT can be concluded, that is, tensile strain weakens the binding of reactive intermediates, while compressive strain results in stronger binding.

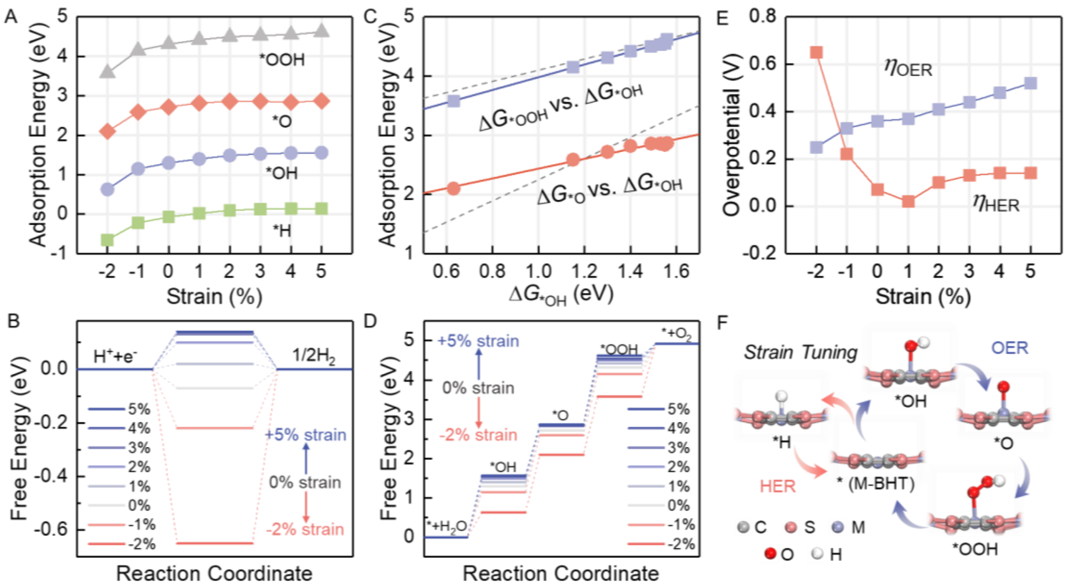

Fig. 5. (a) Strain-induced adsorption energy of *H, *OH, *O, and *OOH on Rh-BHT. The applied strain ranges from -2% to +5%. (b) Free energy diagrams of HER on strained Rh-BHT. (c) Strain effect on scaling relations between the ΔG_{*O} and ΔG_{*OH},

as well as ΔG_{*OOH} and ΔG_{*OH}. The unstrained scaling relations are plotted in dashed lines for comparison. (d) Free energy diagrams of OER on strained Rh-BHT. (e) The strain-overpotential correlation for HER and OER on Rh-BHT. (f) Illustration of the strain-promoted overall water splitting on M-BHT.

The strain-adsorption correlation on Rh-BHT is presented in **Fig. 5a**. The detailed adsorption energies of *H, *OH, *O, and *OOH on strained Rh-BHT are listed in **Table S7**. The strain-induced binding variation of reactive intermediates can efficiently tune the electrocatalytic activity. As shown in **Fig. 5b**, the compressive (tensile) strain strengthens (weakens) the adsorption of HER intermediate *H on Rh-BHT. The desorption of H_2 is the PDS under $\varepsilon \leq +1\%$, while the HER activity is limited by the process of *H adsorption under $\varepsilon \geq +2\%$. Especially, Rh-BHT with +1% tensile strain reaches better adsorption energy of *H (0.02 eV), compared with the unstrained ΔG_{*H} of -0.07 eV. Therefore, the +1% tensile strain leads to the largely enhanced HER performance for Rh-BHT.

Moreover, the adsorption energy variation of *O significantly differs from that of *OH and *OOH when the strain effect is introduced, which changes the former scaling relations among *OH, *O, and *OOH (**Fig. 5c**). Because the step of *O → *OOH is the PDS for unstrained Rh-BHT and strain modulates *O and *OOH adsorption in various degrees, the strained OER volcano peak reaches much higher than the former peak, as shown in **Fig. S12**. The energy change of each OER elementary step on strained Rh-BHT is listed in **Table S8**. It is demonstrated that OER activity is facilitated with the compressive strain, but gets more sluggish with the tensile strain (**Fig. 5d**).

Consequently, the lowest OER overpotential of 0.25 V can be achieved on strained Rh-BHT when ε = -2%.

The HER/OER overpotentials on strained Rh-BHT are summarized in **Fig. 5e**. The strain-overpotential correlation of HER is reversed volcano-shaped, while a linear strain-overpotential correlation of OER emerges. Notably, the +1% tensile strained Rh-BHT exhibits the promoted overall water splitting performance with the HER/OER overpotential of 0.02/0.37 V, compared with the unstrained Rh-BHT of 0.07/0.36 V. Additionally, the HER/OER activity on the strained Ir-BHT is studied to demonstrate the universality of the strain-promoted effect on M-BHT. **Fig. S13** suggests that the -1% compressive strained Ir-BHT can exert the enhanced performance for overall water splitting with η_{HER}/η_{OER} of 0.11/0.43 V, compared with the unstrained Ir-BHT of 0.23/0.47 V. Therefore, the strain-tuning method is an effective and universal strategy to modulate the adsorption of intermediates and boost catalytic activity (**Fig. 5f**).

4. Conclusions

In summary, the feasibility of electrocatalytic HER and OER performance on M-BHT has been demonstrated by using first-principles calculations. Owing to the covalent M-S_4 interactions and in-plane π-d conjugation, M-BHT frameworks can exhibit both high stability and superior conductivity. Moreover, Rh-BHT shows the bifunctional HER/OER activity with the η_{HER}/η_{OER} of 0.07/0.36 V, thereby considered a promising candidate for overall water splitting. Furthermore, the biaxial strain is applied on Rh-BHT to assess the strain effect on the HER/OER performance. It is suggested that the compressive strain can enhance intermediates adsorption and the tensile strain is the opposite, resulting in the tunable catalytic activity. Especially, the strain-promoted HER/OER performance (η_{HER}/η_{OER} = 0.02/0.37 V) is detected on the +1% tensile strained Rh-BHT. Thus, the conductive M-BHT frameworks are a new group of electrocatalysts for overall water splitting and the rational strain tuning will further promote the catalytic activity. This work will facilitate the application of the conductive 2D MOFs and guide the design of efficient catalysts with strain engineering.

CRediT authorship contribution statement

Xiting Wang: Conceptualization, Writing-Original Draft, Visualization. **Huan Niu**: Validation, Writing-Review&Editing. **Xuhao Wan**: Software, Resources, Formal analysis, Writing-Review&Editing. **Zhaofu Zhang**: Visualization, Investigation. **Ryan Wang**: Writing-Review&Editing. **Yuzheng Guo**: Conceptualization, Writing-Review&Editing, Supervision, Project administration.

Declaration of Competing Interest

The authors declare that they have no known competing financial interests or personal relationships that could have appeared to influence the work reported in this paper.

Acknowledgement

We thank the financial support from Wuhan University. Computational resources were provided by the Supercomputing Center of Wuhan University.

Appendix A. Supplementary data

Supplementary materials to this article can be found online.

References

[1] S. Chu, A. Majumdar, Opportunities and challenges for a sustainable energy future, Nature, 488 (2012), pp. 294-303.
[2] A. Landman, H. Dotan, G.E. Shter, M. Wullenkord, A. Houaijia, A. Maljusch, G.S. Grader, A. Rothschild, Photoelectrochemical water splitting in separate oxygen and hydrogen cells, Nat. Mater., 16 (2017), pp. 646-651.
[3] F. Yu, H. Zhou, Y. Huang, J. Sun, F. Qin, J. Bao, W.A. Goddard, S. Chen, Z. Ren, High-performance bifunctional porous non-noble metal phosphide catalyst for overall water splitting, Nat. Commun., 9 (2018), pp. 1-9.
[4] J. Kibsgaard, I. Chorkendorff, Considerations for the scaling-up of water splitting catalysts, Nat. Energy, 4 (2019), pp. 430-433.
[5] I. Roger, M.A. Shipman, M.D. Symes, Earth-abundant catalysts for electrochemical and photoelectrochemical water splitting, Nat. Rev. Chem., 1 (2017), pp. 1-13.
[6] Y. Ping, R.J. Nielsen, W.A. Goddard III, The reaction mechanism with free energy barriers at constant potentials for the oxygen evolution reaction at the IrO_2 (110) surface, J. Am. Chem. Soc., 139 (2017), pp. 149-155.
[7] J. Jia, S. Wei, Q. Cai, J. Zhao, Two-dimensional IrN_2 monolayer: An efficient bifunctional electrocatalyst for oxygen reduction and oxygen evolution reactions, J. Colloid Interface Sci., 600 (2021), pp. 711-718.
[8] X. Li, Z. Su, Z. Zhao, Q. Cai, Y. Li, J. Zhao, Single Ir atom anchored in pyrrolic-N_4 doped graphene as a promising bifunctional electrocatalyst for the ORR/OER: a computational study, J. Colloid Interface Sci., 607 (2022), pp. 1005-1013.
[9] D. Voiry, H. Yamaguchi, J. Li, R. Silva, D.C. Alves, T. Fujita, M. Chen, T. Asefa, V.B. Shenoy, G. Eda, Enhanced catalytic activity in strained chemically exfoliated WS_2 nanosheets for hydrogen evolution, Nat. Mater., 12 (2013), pp. 850-855.
[10] B. Hinnemann, P.G. Moses, J. Bonde, K.P. Jørgensen, J.H. Nielsen, S. Horch, I. Chorkendorff, J.K. Nørskov, Biomimetic hydrogen evolution: MoS_2 nanoparticles as catalyst for hydrogen evolution, J. Am. Chem. Soc., 127 (2005), pp. 5308-5309.
[11] J. Suntivich, K.J. May, H.A. Gasteiger, J.B. Goodenough, Y. Shao-Horn, A perovskite oxide optimized for oxygen evolution catalysis from molecular orbital principles, Science, 334 (2011), pp. 1383-1385.
[12] C. Kuai, Z. Xu, C. Xi, A. Hu, Z. Yang, Y. Zhang, C.-J. Sun, L. Li, D. Sokaras, C. Dong, Phase segregation reversibility in mixed-metal hydroxide water oxidation catalysts, Nat. Catal., 3 (2020), pp. 743-753.
[13] X. Lv, W. Wei, H. Wang, B. Huang, Y. Dai, Holey graphitic carbon nitride (g-CN) supported bifunctional single atom electrocatalysts for highly efficient overall water splitting, Appl. Catal., B, 264 (2020), pp. 118521.
[14] H. Wang, H.-W. Lee, Y. Deng, Z. Lu, P.-C. Hsu, Y. Liu, D. Lin, Y. Cui, Bifunctional non-noble metal oxide nanoparticle electrocatalysts through lithium-induced conversion for overall water splitting, Nat. Commun., 6 (2015), pp. 1-8.
[15] Y. Jia, L. Zhang, G. Gao, H. Chen, B. Wang, J. Zhou, M.T. Soo, M. Hong, X. Yan, G. Qian, A heterostructure coupling of exfoliated Ni-Fe hydroxide nanosheet and defective graphene as a bifunctional electrocatalyst for overall water splitting, Adv.

Mater., 29 (2017), pp. 1700017.
[16] Z. Huang, L. He, W. Zhang, W. Huang, Q. Mo, L. Yang, Q. Fu, Q. Gao, Nickel sulfide-oxide heterostructured electrocatalysts: Bi-functionality for overall water splitting and in-situ reconstruction, J. Colloid Interface Sci., 622 (2022), pp. 728-737.
[17] Y. He, W. Zhou, G. Qian, B. Chen, Methane storage in metal–organic frameworks, Chem. Soc. Rev., 43 (2014), pp. 5657-5678.
[18] A. Bavykina, N. Kolobov, I.S. Khan, J.A. Bau, A. Ramirez, J. Gascon, Metal–Organic Frameworks in Heterogeneous Catalysis: Recent Progress, New Trends, and Future Perspectives, Chem. Rev., 120 (2020), pp. 8468-8535.
[19] H. Furukawa, K.E. Cordova, M. O'Keeffe, O.M. Yaghi, The chemistry and applications of metal-organic frameworks, Science, 341 (2013), pp. 1230444.
[20] L. Jiao, Y. Wang, H.L. Jiang, Q. Xu, Metal-organic frameworks as platforms for catalytic applications, Adv. Mater., 30 (2018), pp. 1703663.
[21] S. Zheng, H. Zhou, H. Xue, P. Braunstein, H. Pang, Pillared-layer Ni-MOF nanosheets anchored on Ti_3C_2 MXene for enhanced electrochemical energy storage, J. Colloid Interface Sci., 614 (2022), pp. 130-137.
[22] J. Liu, D. Zhu, C. Guo, A. Vasileff, S.Z. Qiao, Design strategies toward advanced MOF-derived electrocatalysts for energy-conversion reactions, Adv. Energy Mater., 7 (2017), pp. 1700518.
[23] Z. Wang, Z. Yu, J. Zhao, Computational screening of a single transition metal atom supported on the C_2N monolayer for electrochemical ammonia synthesis, Phys. Chem. Chem. Phys., 20 (2018), pp. 12835-12844.
[24] S. Zhao, Y. Wang, J. Dong, C.-T. He, H. Yin, P. An, K. Zhao, X. Zhang, C. Gao, L. Zhang, Ultrathin metal-organic framework nanosheets for electrocatalytic oxygen evolution, Nat. Energy, 1 (2016), pp. 1-10.
[25] N. Kornienko, Y. Zhao, C.S. Kley, C. Zhu, D. Kim, S. Lin, C.J. Chang, O.M. Yaghi, P. Yang, Metal-organic frameworks for electrocatalytic reduction of carbon dioxide, J. Am. Chem. Soc., 137 (2015), pp. 14129-14135.
[26] J. Zhang, Z. Zhou, F. Wang, Y. Li, Y. Jing, Two-Dimensional Metal Hexahydroxybenzene Frameworks as Promising Electrocatalysts for an Oxygen Reduction Reaction, ACS Sustainable Chem. Eng., 8 (2020), pp. 7472-7479.
[27] Y. Ji, H. Dong, C. Liu, Y. Li, Two-dimensional π-conjugated metal-organic nanosheets as single-atom catalysts for the hydrogen evolution reaction, Nanoscale, 11 (2019), pp. 454-458.
[28] I. Stassen, N. Burtch, A. Talin, P. Falcaro, M. Allendorf, R. Ameloot, An updated roadmap for the integration of metal-organic frameworks with electronic devices and chemical sensors, Chem. Soc. Rev., 46 (2017), pp. 3185-3241.
[29] A.A. Talin, A. Centrone, A.C. Ford, M.E. Foster, V. Stavila, P. Haney, R.A. Kinney, V. Szalai, F. El Gabaly, H.P. Yoon, Tunable electrical conductivity in metal-organic framework thin-film devices, Science, 343 (2014), pp. 66-69.
[30] J. Park, A.C. Hinckley, Z. Huang, D. Feng, A.A. Yakovenko, M. Lee, S. Chen, X. Zou, Z. Bao, Synthetic routes for a 2D semiconductive copper hexahydroxybenzene metal-organic framework, J. Am. Chem. Soc., 140 (2018), pp. 14533-14537.
[31] T. Kambe, R. Sakamoto, K. Hoshiko, K. Takada, M. Miyachi, J.-H. Ryu, S. Sasaki,

J. Kim, K. Nakazato, M. Takata, π-Conjugated nickel bis(dithiolene) complex nanosheet, J. Am. Chem. Soc., 135 (2013), pp. 2462-2465.
[32] J.-H. Dou, L. Sun, Y. Ge, W. Li, C.H. Hendon, J. Li, S. Gul, J. Yano, E.A. Stach, M. Dincă, Signature of metallic behavior in the metal-organic frameworks M_3(hexaiminobenzene)$_2$ (M= Ni, Cu), J. Am. Chem. Soc., 139 (2017), pp. 13608-13611.
[33] Y. Cui, J. Yan, Z. Chen, J. Zhang, Y. Zou, Y. Sun, W. Xu, D. Zhu, $[Cu_3(C_6Se_6)]_n$: The First Highly Conductive 2D π-d Conjugated Coordination Polymer Based on Benzenehexaselenolate, Adv. Sci., 6 (2019), pp. 1802235.
[34] M.G. Campbell, D. Sheberla, S.F. Liu, T.M. Swager, M. Dincă, Cu_3(hexaiminotriphenylene)$_2$: an electrically conductive 2D metal-organic framework for chemiresistive sensing, Angew. Chem. Int. Ed., 54 (2015), pp. 4349-4352.
[35] X. Huang, P. Sheng, Z. Tu, F. Zhang, J. Wang, H. Geng, Y. Zou, C.-a. Di, Y. Yi, Y. Sun, A two-dimensional π-d conjugated coordination polymer with extremely high electrical conductivity and ambipolar transport behaviour, Nat. Commun., 6 (2015), pp. 1-8.
[36] Y.-C. Wang, C.-H. Chiang, C.-M. Chang, H. Maeda, N. Fukui, I.-T. Wang, C.-Y. Wen, K.-C. Lu, S.-K. Huang, W.-B. Jian, C.-W. Chen, K. Tsukagoshi, H. Nishihara, Two-Dimensional Bis(dithiolene)iron(II) Self-Powered UV Photodetectors with Ultrahigh Air Stability, Adv. Sci., 8 (2021), pp. 2100564.
[37] X. Fan, S. Tan, J. Yang, Y. Liu, W. Bian, F. Liao, H. Lin, Y. Li, From Theory to Experiment: Cascading of Thermocatalysis and Electrolysis in Oxygen Evolution Reactions, ACS Energy Lett., 7 (2021), pp. 343-348.
[38] Y. Sun, X. Huang, Y. Jin, Y. Li, Z. Li, Y. Zou, Y. Sun, W. Xu, Highly Conductive Organic-Inorganic Hybrid Silver Sulfide with 3D Silver-Sulfur Networks Constructed from Benzenehexathiol: Structural Topology Regulation via Ligand Oxidation, lnorg. Chem., 61 (2022), pp. 5060-5066.
[39] I.-F. Chen, C.-F. Lu, W.-F. Su, Highly conductive 2D metal-organic framework thin film fabricated by liquid-liquid interfacial reaction using one-pot-synthesized benzenehexathiol, Langmuir, 34 (2018), pp. 15754-15762.
[40] D. Xing, Y. Wang, P. Zhou, Y. Liu, Z. Wang, P. Wang, Z. Zheng, H. Cheng, Y. Dai, B. Huang, Co_3(hexaiminotriphenylene)$_2$: A conductive two-dimensional π-d conjugated metal-organic framework for highly efficient oxygen evolution reaction, Appl. Catal., B, 278 (2020), pp. 119295.
[41] H. Zhong, K.H. Ly, M. Wang, Y. Krupskaya, X. Han, J. Zhang, J. Zhang, V. Kataev, B. Büchner, I.M. Weidinger, A Phthalocyanine-Based Layered Two-Dimensional Conjugated Metal-Organic Framework as a Highly Efficient Electrocatalyst for the Oxygen Reduction Reaction, Angew. Chem. Int. Ed., 131 (2019), pp. 10787-10792.
[42] H. Zhong, M. Ghorbani-Asl, K.H. Ly, J. Zhang, J. Ge, M. Wang, Z. Liao, D. Makarov, E. Zschech, E. Brunner, Synergistic electroreduction of carbon dioxide to carbon monoxide on bimetallic layered conjugated metal-organic frameworks, Nat. Commun., 11 (2020), pp. 1-10.
[43] J. Liu, D. Yang, Y. Zhou, G. Zhang, G. Xing, Y. Liu, Y. Ma, O. Terasaki, S. Yang, L. Chen, Tricycloquinazoline-Based 2D Conductive Metal-Organic Frameworks as Promising Electrocatalysts for CO_2 Reduction, Angew. Chem. Int. Ed., 60 (2021), pp.

14473-14479.
[44] G. Kresse, J. Furthmüller, Efficient iterative schemes for ab initio total-energy calculations using a plane-wave basis set, Phys. Rev. B, 54 (1996), pp. 11169.
[45] J.P. Perdew, K. Burke, M. Ernzerhof, Generalized gradient approximation made simple, Phys. Rev. Lett., 77 (1996), pp. 3865.
[46] S. Grimme, Semiempirical GGA-type density functional constructed with a long-range dispersion correction, J. Comput. Chem., 27 (2006), pp. 1787-1799.
[47] K. Mathew, R. Sundararaman, K. Letchworth-Weaver, T. Arias, R.G. Hennig, Implicit solvation model for density-functional study of nanocrystal surfaces and reaction pathways, J. Chem. Phys., 140 (2014), pp. 084106.
[48] W. Tang, E. Sanville, G. Henkelman, A grid-based Bader analysis algorithm without lattice bias, J. Phys.: Condens. Matter, 21 (2009), pp. 084204.
[49] R. Nelson, C. Ertural, J. George, V.L. Deringer, G. Hautier, R. Dronskowski, LOBSTER: Local orbital projections, atomic charges, and chemical-bonding analysis from projector-augmented-wave-based density-functional theory, J. Comput. Chem., 41 (2020), pp. 1931-1940.
[50] J.K. Nørskov, J. Rossmeisl, A. Logadottir, L. Lindqvist, J.R. Kitchin, T. Bligaard, H. Jónsson, Origin of the Overpotential for Oxygen Reduction at a Fuel-Cell Cathode, J. Phys. Chem. B, 108 (2004), pp. 17886-17892.
[51] J.K. Nørskov, T. Bligaard, A. Logadottir, J. Kitchin, J.G. Chen, S. Pandelov, U. Stimming, Trends in the exchange current for hydrogen evolution, J. Electrochem. Soc., 152 (2005), pp. J23.
[52] H. Niu, X. Wan, X. Wang, C. Shao, J. Robertson, Z. Zhang, Y. Guo, Single-Atom Rhodium on Defective g-C_3N_4: A Promising Bifunctional Oxygen Electrocatalyst, ACS Sustainable Chem. Eng., 9 (2021), pp. 3590-3599.
[53] X. Guo, J. Gu, S. Lin, S. Zhang, Z. Chen, S. Huang, Tackling the activity and selectivity challenges of electrocatalysts toward the nitrogen reduction reaction via atomically dispersed biatom catalysts, J. Am. Chem. Soc., 142 (2020), pp. 5709-5721.
[54] X. Guo, S. Lin, J. Gu, S. Zhang, Z. Chen, S. Huang, Simultaneously achieving high activity and selectivity toward two-electron O_2 electroreduction: the power of single-atom catalysts, ACS Catal., 9 (2019), pp. 11042-11054.
[55] S. Nosé, A unified formulation of the constant temperature molecular dynamics methods, J. Chem. Phys., 81 (1984), pp. 511-519.
[56] B. Huang, N. Zhou, X. Chen, W.J. Ong, N. Li, Insights into the electrocatalytic hydrogen evolution reaction mechanism on two-dimensional transition-metal carbonitrides (MXene), Chem. - Eur. J., 24 (2018), pp. 18479-18486.
[57] H. Xu, D. Cheng, D. Cao, X.C. Zeng, A universal principle for a rational design of single-atom electrocatalysts, Nat. Catal., 1 (2018), pp. 339-348.
[58] G. Gao, A.P. O'Mullane, A. Du, 2D MXenes: a new family of promising catalysts for the hydrogen evolution reaction, ACS Catal., 7 (2017), pp. 494-500.
[59] X. Lv, W. Wei, P. Zhao, D. Er, B. Huang, Y. Dai, T. Jacob, Oxygen-terminated BiXenes and derived single atom catalysts for the hydrogen evolution reaction, J. Catal., 378 (2019), pp. 97-103.
[60] I.C. Man, H.Y. Su, F. Calle-Vallejo, H.A. Hansen, J.I. Martínez, N.G. Inoglu, J.

Kitchin, T.F. Jaramillo, J.K. Nørskov, J. Rossmeisl, Universality in oxygen evolution electrocatalysis on oxide surfaces, ChemCatChem, 3 (2011), pp. 1159-1165.
[61] C. Ling, L. Shi, Y. Ouyang, X.C. Zeng, J. Wang, Nanosheet supported single-metal atom bifunctional catalyst for overall water splitting, Nano Lett., 17 (2017), pp. 5133-5139.
[62] H. Niu, X. Wang, C. Shao, Y. Liu, Z. Zhang, Y. Guo, Revealing the oxygen reduction reaction activity origin of single atoms supported on g-C_3N_4 monolayers: a first-principles study, J. Mater. Chem. A, 8 (2020), pp. 6555-6563.
[63] Z. Fu, C. Ling, J. Wang, A $Ti_3C_2O_2$ supported single atom, trifunctional catalyst for electrochemical reactions, J. Mater. Chem. A, 8 (2020), pp. 7801-7807.
[64] J.R. Kitchin, J.K. Nørskov, M.A. Barteau, J. Chen, Role of strain and ligand effects in the modification of the electronic and chemical properties of bimetallic surfaces, Phys. Rev. Lett., 93 (2004), pp. 156801.
[65] M. Luo, Z. Zhao, Y. Zhang, Y. Sun, Y. Xing, F. Lv, Y. Yang, X. Zhang, S. Hwang, Y. Qin, PdMo bimetallene for oxygen reduction catalysis, Nature, 574 (2019), pp. 81-85.
[66] H. Wang, S. Xu, C. Tsai, Y. Li, C. Liu, J. Zhao, Y. Liu, H. Yuan, F. Abild-Pedersen, F.B. Prinz, Direct and continuous strain control of catalysts with tunable battery electrode materials, Science, 354 (2016), pp. 1031-1036.
[67] T. He, W. Wang, F. Shi, X. Yang, X. Li, J. Wu, Y. Yin, M. Jin, Mastering the surface strain of platinum catalysts for efficient electrocatalysis, Nature, 598 (2021), pp. 76-81.

Highlights

1) The extended in-plane π-d conjugation between metal centers and organic linkers guarantees superior conductivity of the designed M-BHT.

2) Rh-BHT is screened as the promising bifunctional HER/OER catalyst with the low overpotentials of 0.07/0.36 V.

3) The compressive (tensile) strain can effectively enhance (weaken) intermediates adsorption, leading to the tunable HER/OER activity.

4) The strain-promoted overall water splitting performance can be reached on the +1% tensile strained Rh-BHT.

Graphical Abstract